· Article ·
doi: 10.13679/j.advps.2014.2.00113

Advances in Polar Science
June 2014 Vol. 25 No. 2: 113-120

Numerical simulation of the dynamic characteristics of flow fields under ice

SUN Hui, LU Peng* & LI Zhijun

State Key Laboratory of Coastal and Offshore Engineering, Dalian University of Technology, Dalian 116024, China

Received 30 July 2013; accepted 7 March 2014

Abstract Atmospheric and oceanic drag are the main environmental forces controlling sea ice drift. Oceanic drag includes the form drag generated by water pressure gradients on the side of ice floes or on ice ridges, and the skin friction generated by viscous flow on the bottom of ice floes. In this study, we carried out a two-dimensional numerical simulation using FLUENT software to investigate the characteristics of dynamic flow under ice with a smooth undersurface. We studied water drag and flow field distribution below the ice under different conditions of ice draft and flow velocity, and the results agreed well with data from laboratory-based physical modeling tests, demonstrating the ability of the numerical model to reproduce the dynamic interactions between sea ice and the flow field. The degree of distortion in the flow field caused by ice increased as the ice draft increased. Vortexes occurred in the wake field of the floe, and the centers of the vortexes moved away from the ice with increasing ice draft. The simulated drag of water on ice showed a clear linear relationship with the square of the flow velocity.

Keywords **FLUENT, ice dynamics, drag, flow field, numerical simulation**

Citation: Sun H, Lu P, Li Z J. Numerical simulation of the dynamic characteristics of flow fields under ice. Adv Polar Sci, 2014, 25:113-120, doi: 10.13679/j.advps.2014.2.00113

1 Introduction

Sea ice drift is an important part of the global water circulation, and also has a major impact on global climate change and on human activities in ice-infested waters. The study of sea ice dynamics focuses on drift variations, momentum transfer, fracture, overlap, and the accumulation of sea ice under the actions of oceanic and atmospheric forcing[1]. Sea ice dynamics models that include many of the morphological parameters of sea ice are used to describe the dynamic interactions among sea ice, atmosphere, and ocean, and wind and flow drag forces play key roles in these dynamic interactions. According to the drag partition theory, the total drag includes form drag generated by pressure gradients on the sides of ice floes or on ice ridges, and the skin friction caused by viscous flow on the undersurface of ice floes. Ice-ocean and air-ice drag coefficients, usually with an order of magnitude of 10^{-3}[2-6], describe the horizontal momentum exchange on ice-ocean and air-ice interfaces, and are important parameters within sea ice dynamics models. The accuracy of these parameters therefore directly affects the accuracy of dynamics models[7] and many previous studies have investigated the effects of these parameters on model outcomes[3-4].

In addition to the traditional methods of determining sea ice drag coefficients including the eddy correlation method, the profile method, and the momentum method[1], parameterization of drag coefficients has become a new research focus[5-6,8-10]. For example, Arya[5-6] divided total drag into form drag on ice ridges and skin friction on the ice surface, and determined the relationship between total drag and ridge height, distribution, and ice surface roughness. Hanssen-Bauer and Gjessing[8] divided the total drag force into form drag on the ice edge and skin friction on the ice surface, ignoring ice ridges, and calculated the relationship between the drag coefficient and ice thickness, concentration,

* Corresponding author (email: lupeng@dlut.edu.cn)

and size. Mai et al.[9] combined the results of previous studies, and built a relatively complete parameterization of the sea ice drag coefficient by taking into account ice ridge form drag, ice side form drag, and surface skin friction. Birnbaum and Lüpkes[11] derived a parameterization of surface drag over the marginal ice zone (MIZ) which accounted for the form drag caused by floe edges and combined it with a so-called flux averaging method for the determination of surface fluxes over inhomogeneous terrain. Lüpkes and Birnbaum[12] compared two parameterization schemes for drag coefficients, based on different principles (flux averaging and parameter averaging), and found the resulting drag coefficients differed only slightly in the case of neutral and stable stratification. Lüpkes et al.[13] derived a hierarchy of parameterization for neutral 10 m drag coefficients over polar sea ice with different morphology regimes based on a partitioning concept that splits the total surface drag into the contributions of skin drag and form drag. In these previous studies, the form drag coefficient on the ice edge is a constant (~1) according to the theory of fluid mechanics[14], and the form drag coefficient on ice ridges ($\sim 10^{-3}$)[15] and the skin friction coefficient on ice surfaces ($\sim 10^{-3}$)[10] are variables associated with ridge slope and surface roughness, respectively, based on *in-situ* measurements. These studies have focused on air-ice interfaces, mainly because the atmospheric boundary layer over the sea ice and ice surface morphology are easy to observe and easy to compare with parameterization results. For the ice-ocean interface, only Lu et al.[10] carried out a theoretical study on the ice-ocean drag coefficient, and established a relationship between the oceanic drag coefficient with floe and ridge geometries. However, because of the lack of observations in the oceanic boundary layer some important dynamic mechanisms among the ice-ocean interactions, including the wake effect behind floe edges and ridge keels, were still assumed to be similar to those in the air-ice interface.

To address this deficit, physical modeling tests have been conducted to reproduce the flow field under sea ice using particle image velocimetry (PIV)[10,16-17]. To a certain extent, this compensates for the lack of field observations on ice-ocean interactions. In addition, some qualitative characteristics of the flow field and relationships among ice geometric parameters, skin, and form drag have been determined. However, because of the limitations in laboratory experimental conditions, it has been difficult to establish a complete quantitative law using experimental data, and it is therefore necessary to augment the experimental data on flow fields under ice using numerical simulations.

In the present study, we carried out a numerical simulation of flow fields under ice using FLUENT software and compared the output with previous experimental results. This approach will not only verify the validity of the numerical model, but will also enable the observation of phenomena that may not be seen in physical experiments, thus improving the understanding of dynamic processes and physical mechanisms in ice-ocean interactions. FLUENT is one of the most comprehensive and extensively applied software packages used in computational fluid dynamics (CFD). It can be used to analyze two-dimensional flat surfaces, ax-symmetric and three-dimensional flow, and can also be used to complete flow analysis in multiple reference systems, for steady and unsteady flow analysis, incompressible and compressible flow calculations, laminar and turbulent flow simulations, and multiphase flow[18]. There are many examples that demonstrate that numerical simulations using FLUENT can accurately forecast the dynamic characteristics of flow fields, and provide valuable support to physical modeling tests [19-20].

2 Mathematical model

In previous physical modeling tests, the flow flume was 22 m long, 0.45 m wide, and 0.6 m deep, and the water in the flume was 0.4 m deep. The floe model used in the tests had a smooth undersurface, was 0.45 m long, 0.35 m wide and 0.15 m deep, and was installed on a platform that could move vertically to change the draft[16]. The flume and floe model are shown in Figure 1.

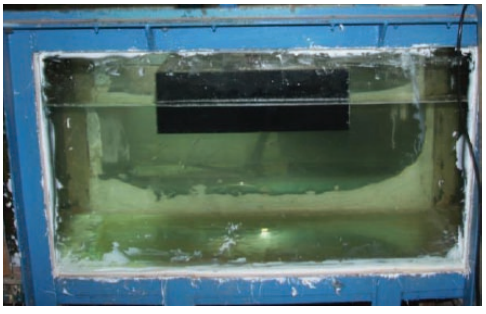

Figure 1 The flume and floe model used in the physical modeling tests[16].

As is the case in most laboratory experiments it was not possible to match all the relevant parameters[21]. For flow fields under sea ice, flow viscosity and the associated vortex, and skin friction are the primary properties that need to be considered during modeling. Therefore, the similarity of Reynolds number (*Re*) was employed in the physical modeling tests instead of the similarity of Froude number (*Fr*) that takes more account of gravity-induced motion. According to the drift velocity (0.01–1 $m \cdot s^{-1}$)[2,22] and the mean thickness (2–8 m)[2,22] of Arctic sea ice, the *Re* of the flow field falls within a large range of 10^4–10^6. In the MIZ, which is usually made up of small floes of first-year ice and melted multi-year ice, the ice thickness is generally within a range of 0.5–2 m[23-24], producing a *Re* in the range of 10^3–10^4. As far as possible, the physical modeling tests in this study were set up to produce a similar *Re* to the natural Arctic MIZ[22] (Table 1) because the effects of form drag on ice and the drag coefficient parameterization are more significant for small floes in the MIZ than for regions consisting of large floes or continuous ice cover[10].

To ensure a useful comparison with the physical modeling tests the dimensions of the employed mathematical

model in the numerical simulation were completely consistent with those of the physical model. Taking into account the symmetry of the flow field and the slight variations along the width of the floe model, the simulation was simplified to a two-dimensional flow problem. That is, the vertical cross section along the length of the flume was chosen as the computational domain of the numerical simulation, as shown in Figure 2. To ensure a fully developed wake flow on the lee side of the ice floe, the floe model was placed one third of the way along the length of the flume and the dimensions of the model were set so that DE/EF >30 (Figure 2), agreeing with the general conditions for a fully developed wake flow.

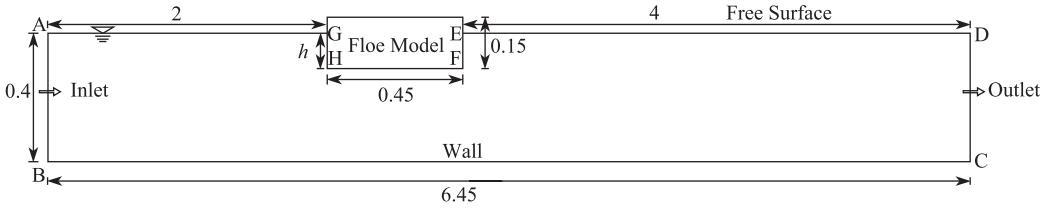

Figure 2 The computational domain of the flow field under ice in the numerical simulation (Unit: m).

3 Grid and boundary conditions

A reasonable design and high grid quality in the computational domain are pre-conditions for CFD because the grid quality has a major influence on the accuracy and efficiency of the calculations[25]. The initial grids were generated using GAMBIT software, and the whole domain was divided into different sections based on different accuracy requirements. Unstructured grids were used near the floe model, while structured grids were used in other regions. Boundary layer grids were used on the floe model and flume wall. The grid distribution is shown in Figure 3.

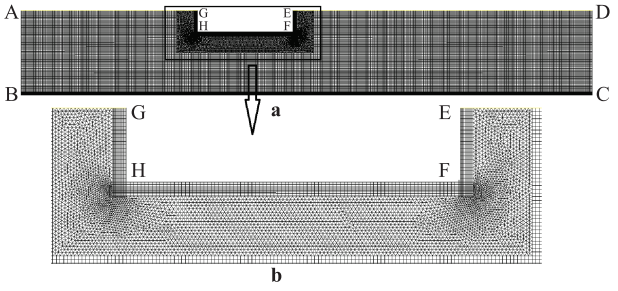

Figure 3 **a**, Grid distribution in the whole computational domain; **b**, grids near the floe model.

In the computational domain (Figure 2), AB is the water inlet, and it has a uniform velocity distribution so a velocity inlet boundary condition was applied at AB. Boundaries BC, GH, HF, FE are solid walls and no-slip wall boundary conditions were used. The outlet DC is described by free outflow conditions, in which the flow rate can be fully developed because the wake flow region behind the ice is sufficiently long. A rigid lid assumption was employed for the free surfaces AG and ED, defining them as symmetry surfaces, namely free-slip walls.

4 Numerical simulation and analysis of results

4.1 Solving methods

A two-dimensional numerical model was subdivided into cells, while the continuity equation and the Navier-Stokes equation were discretized using the finite volume method, and renormalization group (RNG) k-ε turbulence model equations were used to close the equations set. The method of enhanced wall function was used near walls, such as the surfaces of the flume and floe model. Governing equations were solved using a two-dimensional pressure-based solver in a second order, implicit, steady formulation and iterated to achieve a converged solution. Pressure-velocity coupling used the SIMPLEC algorithm. The discretization scheme for pressure used the standard format, while others such as momentum, turbulent kinetic energy, and turbulent dissipation rate were carried out using a second order upwind scheme. The simulation has reached convergence if all residuals are reduced to less than 10^{-4}. In the simulation, the $Re = uh/\upsilon$, where h is the ice draft, u is the inlet flow velocity, and υ is kinematic viscosity of water.

As for the physical modeling tests[16], 40 different calculation conditions were used in the numerical simulation, as shown in Table 1. The relative velocity of ice and water in the physical modeling tests was set in the range of the drift velocity of Arctic sea ice (0.01–0.3 m·s^{-1})[26] by adapting the AC motor frequency, ensuring a realistic setting for the study of sea ice dynamics. There is a linear relationship between the flow velocity and the motor frequency ($u = 0.0069f$), and flow velocities in Table 1 match the motor frequencies at 3 Hz, 5 Hz, 8 Hz, 10 Hz, 15 Hz, 20 Hz, 30 Hz, and 40 Hz. In addition, the ratio of the length to thickness of sea ice is always in the range of 5–10 000[16]. The floe model used here was 45 cm long but its draft was set at 2.5 cm, 5 cm, 7.5 cm, 10 cm, or 12.5 cm, to produce a ratio of length to thickness of 3.6–18, which is basically in the range of natural sea ice but more typical of the smaller ice floes in the MIZ. This range was selected not only because of limitations in the laboratory experimental conditions, but also because of the more obvious effect on wake flow for smaller ice floes[10].

4.2 Flow field analysis

In the dynamic interactions between ice and water, a floe will impose a shadowing effect on the following floes, and the

form drag on the following floes will also be changed by the resultant wake flow, making the wake flow distribution an important component in the parameterization of the sea ice drag coefficient. Therefore, analysis of the flow field mainly focuses on the regions below the ice and in the wake flow.

Table 1 Calculation conditions in the numerical simulation and the corresponding Reynolds number

Flow velocity u/(m·s^{-1}) \ Ice draft h/cm	2.5	5	7.5	10	12.5
0.28	6 144	12 288	18 341	24 575	30 719
0.21	4 608	9 216	13 823	18 431	23 039
0.14	3 072	6 144	9 216	12 288	15 359
0.10	2 304	4 608	6 912	9 216	11 520
0.07	1 536	3 072	4 608	6 144	7 680
0.06	1 229	2 458	3 686	4 915	6 144
0.03	768	1 536	2 304	3 072	3 840
0.02	461	922	1 382	1 843	2 304

The velocity contours of the flow field for five different ice drafts under the maximum inlet velocity are shown in Figure 4. It is clear from Figure 4 that the range of disturbance in the flow field caused by the ice increased with increasing ice draft. Vortexes occurred under the bottom left of the floe model and in the wake field, and both were more obvious for larger ice drafts (Figure 4b). In particular, with increasing ice draft at the same inlet velocity, the vortex in the wake field extended, and its center gradually moved away from the floe model, mainly because the shadowing area of the ice increased with a deeper ice draft generating a lower flow velocity near the lee side of the ice.

To further study the simulated flow velocity distributions in a vertical plane for different ice drafts, four representative vertical profiles of flow velocity were selected from the calculations for each ice draft. Taking into account that the disturbance in the flow field caused by the floe model is restrained to about ±10 cm from the front and rear of the floe model, the selected sections were located 8 cm in front of (section 1) and behind the floe model (section 4), 10 cm from

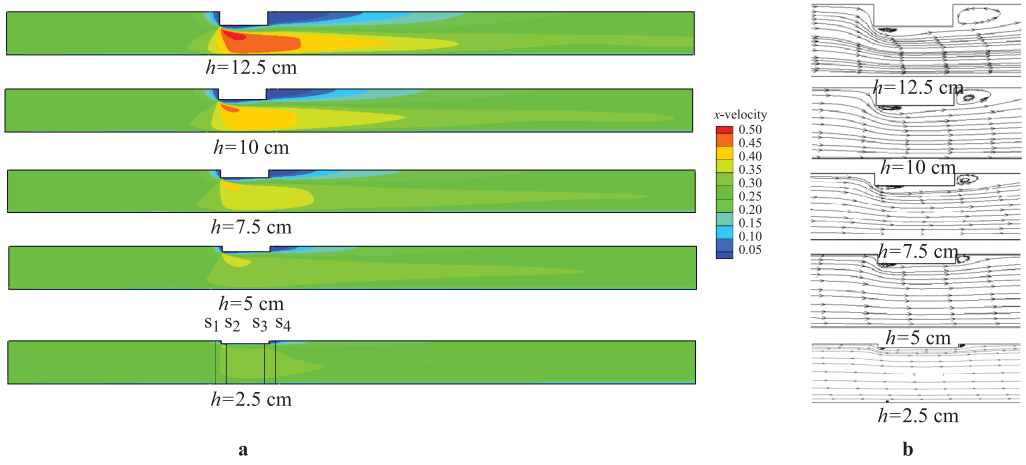

Figure 4 **a**, Contour of flow velocity for five different ice drafts at an inlet velocity of 0.28 m·s^{-1}; **b**, vortexes around the floe model.

the left corner of the ice (section 2), and 5 cm from the right corner (section 3), as shown by S1, S2, S3, and S4 in Figure 4a. The sections were mainly located near the ice model where flow velocity changed significantly.

It is clear from Figure 5 that the simulated flow velocity for section 1 in front of the ice floe model gradually increased to the initial inlet velocity across the water depth, but the increase in rate decreased rapidly when the water depth was below the ice draft. The simulated flow velocities for section 2 and section 3 had larger fluctuations than for section 1, mainly because of the narrow cross-section area and resulting increase in velocity under the floe model, together with the presence of a vortex at the leading edge of the underside of the floe. Section 3 was close to the rear of the floe, where the flow velocity was stable but the variation trend along its depth was roughly similar to that for section 2. Section 4 was in the wake flow field, and negative velocities appeared as a result of the vortex, while the flow velocity was relatively low within the ice draft because of the obvious shadowing effect of the floe model.

Figure 5 also shows the comparisons between the numerical simulation and the physical modeling tests for sections 2 and 3 for ice drafts of 5 cm and 10 cm and for section 4 at five different ice drafts. Overall, the numerical results for sections 2, 3, and 4 agree well with the physical modeling tests across the range of ice drafts, supporting the validity of the model and the reliability of the numerical simulation. However, some deviations between the results of the numerical and physical modeling are obvious for section 4 for Z = 0.1–0.2 m as the ice draft increases, as shown in Figure 5a and 5b. This is mainly because, in these cases, a water depth of 0.1–0.2 m is close to the bottom of the ice floe model, and section 4 is close to the floe model, so the velocity fluctuation caused by the motor vibration was more obvious. However, the deviation was very small with smaller flow fluctuations at drafts of less than 10 cm.

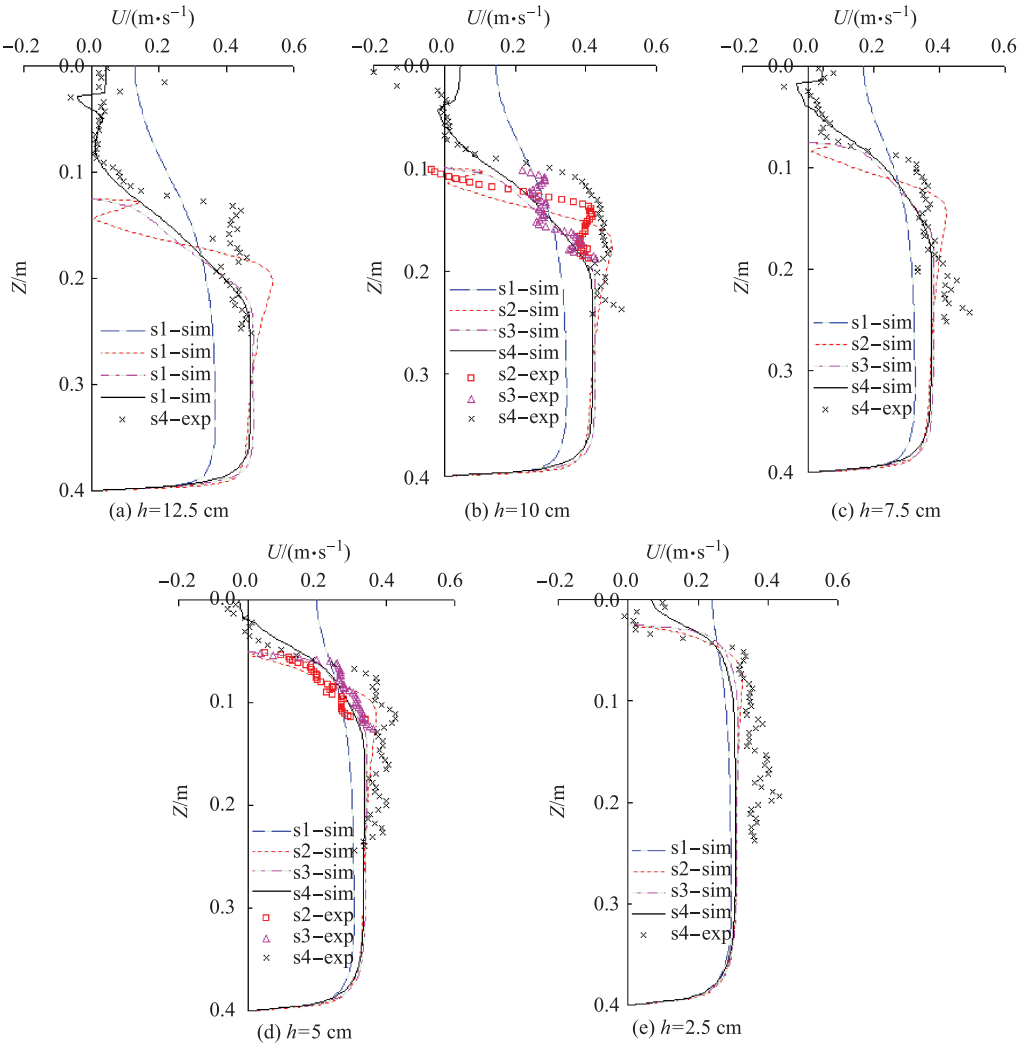

Figure 5 Flow velocity distribution along four vertical profiles (-sim), and comparison with physical modeling tests (-exp) for five different ice drafts at an inlet velocity of 0.28 m·s^{-1}.

4.3 Drag force analysis

According to drag theory, the ice-water drag coefficient C_D can be defined as

$$C_D = \frac{\tau_0}{\rho U^2}$$

where τ_0 is the flow drag stress on the undersurface of the ice, ρ is the flow density, and U is the flow reference speed.

In numerical simulations, the water drag force exerted on the floe model can be obtained by integrating the normal pressure on the ice edge and the skin friction along the undersurface of the ice. Figure 6 shows the calculated total drag force for five ice drafts and eight inlet velocities, and the comparison with the results of the physical modeling tests. It is clear from Figure 6 that the experimental data agreed well with the calculated drag force for ice drafts of 2.5 cm, 5 cm, and 7.5 cm. For larger ice drafts of 10 cm and 12.5 cm, the agreement was acceptable at relatively low flow velocities, but the calculated value became larger than the experimental data as the flow velocity increased. The largest deviation occurred at an ice draft of 12.5 cm and an inlet velocity of 0.28 m·s^{-1}. This can mainly be attributed to the vibration of the floe model in the physical modeling tests, resulting from the effects of motor vibration and the vortex-induced vibration during ice-ocean interactions. In processing the experimental data, high-frequency vibrations are removed using a low-pass filter, and then the mean of the filtered data is taken as the measured drag force, enabling measurement of the missing peak values. The vibration of the floe model is greater for larger ice drafts and flow velocities, so the experimental data after low-pass filtering tend to become lower than the calculated drag force. However, the simulated drag forces in Figure 6 agreed well with the overall trend in the experimental data when the structural vibration was not obvious for small ice drafts and inlet velocities, which also proves the validity of the numerical model.

As seen in Figure 6, the calculated drag force increased with increasing ice draft, and there was a clear linear relationship with the square of flow velocity, agreeing well

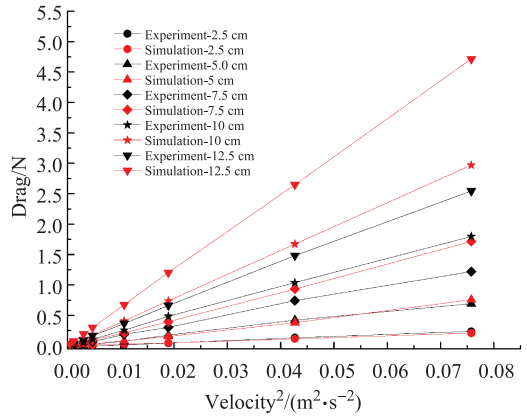

Figure 6 Comparisons of simulated drag forces with the results of physical modeling tests for five different ice drafts and eight inlet flow velocities.

with drag theory[14]. For small ice drafts, drag force increased relatively slowly with increasing flow velocity, but for large ice drafts, the drag force increased more rapidly as the flow velocity increased. The main explanation for this is that a small ice draft has a small ice-edge area exerted by the normal pressure of water, so the form drag is only a small part of the total drag force. Skin friction is mainly related to the floe size and the roughness of the undersurface of the ice, and the form drag is more than 60% of the total drag force for the small floes with thickness/length of $\geqslant 1/100$[10]. Therefore, the total drag increases slowly for small floes. Conversely, for large ice drafts, the form drag on the ice edge increases rapidly with the flow velocity, and the form drag becomes the dominant contributor to the total drag force.

Once the normal pressure on the ice edge and the skin friction along the undersurface of the ice are integrated, the form drag coefficient on ice edge C_1 and the skin friction drag coefficient on ice bottom C_2 can be calculated, and the results under different *Re* and aspect ratios (draft/length) are summarized in Figure 7.

As shown in Figure 7a, the form drag coefficient C_1 increased with an increase in the aspect ratio of ice draft to length. For the same aspect ratio, the variations of C_1 were insensitive to the variations in *Re*. When the aspect ratio was small, the form drag coefficient C_1 decreased then increased with increasing *Re*, but for the large aspect ratio, the variation was minimal. In previous studies on drag partitioning, $C_1 = 1.0$ has always been used for a wide range of *Re*[8,27]. However, in the theory of fluid mechanics[14,28], the generation of the form drag coefficient is largely a result of the liquid viscous effects which result in separations in the boundary layer, thus forming a pressure difference. However, the pressure difference depends on the position of the separation point, which has a relationship with velocity distribution and the shape of the object, and is closely related to the fluid morphogenetic changes caused by the *Re*. In Figure 7b, for the same aspect ratio, the skin friction drag coefficient C_2 decreased with increasing *Re*. When the aspect ratio of ice draft to length increased, the skin friction drag coefficient C_2 first decreased

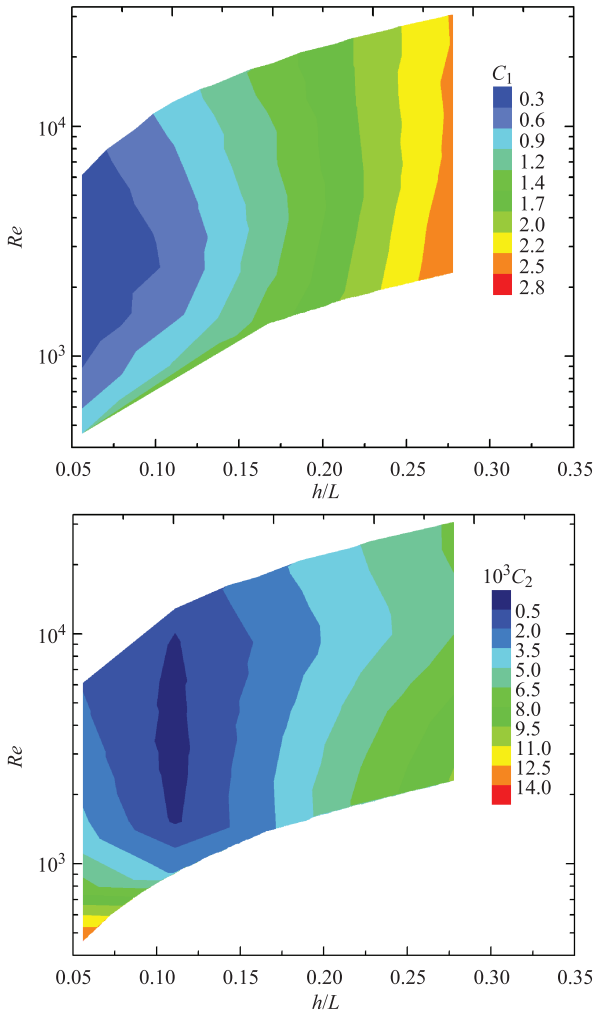

Figure 7 Variations of the form drag coefficient on the ice edge C_1 (**a**), and the skin friction drag coefficient on the undersurface of the ice C_2 (**b**), with the Reynolds number and the ratio of ice draft to length.

and then increased, mainly because the direction of the floe model undersurface shear stress force changed. When $h/L = 0.056$(h=2.5 cm), the vortex around the left corner was not very obvious, the direction of the resultant shear stress at the undersurface was to the horizontal right (horizontal right taken as the positive direction), and the skin friction drag was positive (Figure 8). When h/L=0.11 (h=5 cm), the undersurface viscous stress force underwent a gradual shift in direction, resulting from the increasing scope and strength of the vortex, from the horizontal right to the horizontal left. At this point, the skin friction drag was negative. Subsequently, the skin friction drag increased with increasing ice draft, because of the enhanced vortex and the associated shear stress in the horizontal left direction (Figure 8); therefore, C_2 as shown in Figure 7b follows a parabolic-shaped trend. In addition, the skin friction drag coefficient in Figure 7b was mainly distributed at a magnitude of 10^{-3}. Based on sea ice dynamics modeling and field observations in previous studies[29–31], the skin friction drag coefficient

at the undersurface of the ice usually ranges from 1.0×10^{-4} to 9.9×10^{-2}, and the calculated results from this study were within this range, although closer to the lower limit as a result of the smooth surface, further supporting the reliability of the numerical model.

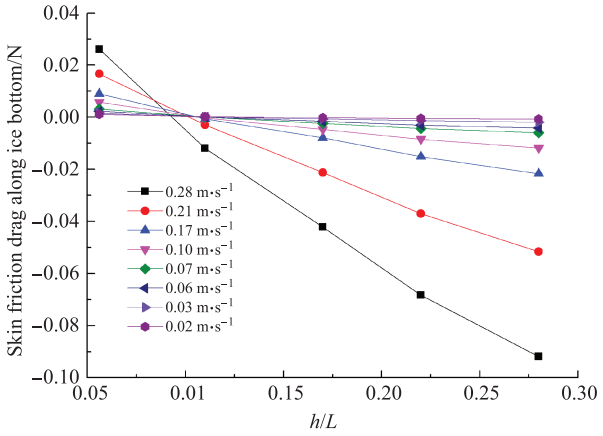

Figure 8 The skin friction drag along the undersurface of the ice at eight velocities and the ratio of ice draft to length.

5 Conclusion

In this paper, the Reynolds-averaged Navier-Stokes equations were taken as the governing equations, and RNG k-ε turbulence equations were used to close governing equations and set up turbulence models to simulate flow fields under ice. The ice drag force and the dynamic characteristics of flow fields under ice were simulated under different flow and ice conditions. We conclude that the area of the flow field disturbed by ice increases with increasing ice draft, but the dependence on variations in flow velocity is not obvious. Vortexes occur in front of the undersurface of the ice and in the wake field behind the lee side of the floe. Because of the shadowing effect of ice, an attenuation zone of flow velocity exists in the wake flow and its range increases with increasing ice draft. At the same flow velocity, the vortexes become larger with increasing ice draft and the centers of the vortexes move away from the ice. Wake effects in ice-ocean interactions are also important hydrodynamic processes that must be considered when determining the drag components.

The results of numerical simulation also reveal that ice drag force has a clear linear relationship with the square of the flow velocity, which is consistent with drag theory. Particularly at low velocity, the numerical results agree well with the measured drag forces in physical modeling tests, proving the feasibility of the model. Based on the theoretical formulas, when the aspect ratio is small, the form drag coefficient C_1 decreases then increases with increasing Re, the skin friction drag coefficient on the undersurface of the ice C_2 has a magnitude mainly in the range of 10^{-3}, agreeing with recently reported values from sea ice modeling and field investigations. The relationship between the sea ice drag coefficients and the Re, the floe aspect ratio, is also presented (Figure 7), and dimensionless parameters are employed, making the results of this study easy to compare with future results from physical modeling tests and *in-situ* observations. Parameterization of sea ice drag coefficients is the final objective of this study, and this will result in a more accurate description of ice drift, but must be based on a thorough understanding of the processes involved in air-ice-ocean interactions. Limitations to the direct measurements of the oceanic boundary layer under ice cover mean deficiencies in the knowledge of ice-ocean dynamic processes must be addressed using laboratory experiments such as physical modeling tests and numerical simulation. Furthermore, numerical simulation can provide more results under different working conditions compared with physical modeling. In this study, the feasibility of numerical simulation was first proven through comparisons with physical modeling, and more simulations will be carried out in the future to improve the numerical model and to obtain more details of the flow field, for example, using ice floes with different undersurface roughness and ice ridges of different inclinations, enabling more quantitative conclusions to provide support for parameterization of the sea ice drag coefficient. In future studies the present parameterization will have the potential to be applied in any coupled ice-ocean model and will enable the investigation of changes in the drag coefficient over a large area such as a numerical grid cell, from an empirical constant to a variable depending on local sea ice conditions. This will lead to a more accurate description of sea ice dynamics and further discussions on these issues will be addressed in a future study.

Acknowledgments This study was supported by the National Natural Science Foundation of China (Grant nos. 41276191 and 40930848).

References

1 Ji S Y, Yue Q J. Project sea ice numerical model and application. Beijing: Science Press, 2011(in Chinese).
2 Leppäranta M. The drift of sea ice. Springer-Praxis Books in Geophysical Science, first eds. Springer-Praxis, 2005, 30-55, 118-138.
3 Christian W C, Martinson D G. Drag coefficients for winter Antarctic pack ice. Journal of Geophysical Research, 1993, 98(C7): 12431-12437, doi: 10.1029/93JC00655.
4 Anderas E L, Claffey K J. Air-ice drag coefficients in the western Weddell Sea: 1. Values deduced from profile measurements. Journal of Geophysical Research, 1995, 100(C3): 4821-4831, doi: 10.1029/94JC02015.
5 Arya S P S. Contribution of form drag on pressure ridges to the air stress on Arctic ice. Journal of Geophysical Research, 1973, 78(30): 7092-7099, doi: 10.1029/JC078i030p07092.
6 Arya S P S. A drag-partition theory for determining the large-scale roughness parameter and wind stress on Arctic pack ice. Journal of Geophysical Research, 1975, 80(24): 3447-3454,doi: 10.1029/JC080i024p03447.
7 Tan B, Lu P, Li Z J, et al. Form drag of ice ridges in winter Weddell Sea, Antarctica. Advances in Water Science, 2012, 23(6): 869-873.
8 Hanssen-Bauer I, Gjessing Y T. Observations and model calculations of aerodynamic drag on sea ice in the Fram Strait. Tellus A, 1988, 40A(2): 151-161, doi:10.1111/j.1600-0870.1988.tb00413.x.

9 Mai S, Wamser C, Kottmeier C. Geometric and aerodynamic roughness of sea ice. Boundary-Layer Meteorology, 1996, 77(3-4): 233-248.
10 Lu P, Li Z J, Cheng B, et al. A parameterization of the ice-ocean drag coefficient. Journal of Geophysical Research, 2011, 116: C07019, doi: 10.1029/2010JC006878.
11 Birnbaum G, Lüpkes C. A new parameterization of surface drag in the marginal sea ice zone. Tellus A, 2002, 54(1): 107-123.
12 Lüpkes C, Birnbaum G. Surface drag in the Arctic marginal sea-ice zone: a comparison of different parameterization concepts. Boundary-layer meteorology, 2005, 117(2):179-211.
13 Lüpkes C, Gryanik V M, Hartmann1 J, et al. A parametrization based on sea ice morphology, of the neutral atmospheric drag coefficients for weather prediction and climate models. Journal of Geophysical Research, 2012, 117(D13): doi: 10.1029/2012JD017630.
14 Hoerner S F. Fluid-dynamic drag.The Author Press, 1965, 3-15.
15 Tan B, Li Z J, Lu P, et al. Morphology of sea ice pressure ridges in the northwestern Weddell Sea in winter. Journal of Geophysical Research, 2012, 117, C6, doi: 10.1029/2011JC007800.
16 Zhang Q. Application of PIV on flow field measurement under floe ice in laboratory modeling. Dalian: Dalian University of Technology, 2009 (in Chinese with English abstract)
17 Bai Y L, Li Z J, Lu P, et al. Optimization and identification on current drag coefficient of isolated floe based on experimental data. Journal of Dalian University of Technology, 2007, 47(6): 885-889 (in Chinese with English abstract).
18 Wang F J. Computational fluid dynamics analysis-CFD software principles and applications. Beijing: Tsinghua University Press, 2004 (in Chinese).
19 Liu X, Ge X F. Application of FLUENT in China. Energy Research and Utilization, 2003, 2: 36-38(in Chinese).
20 Ye M, Wu C, Chen Y L, et al. Application of FLUENT to hydraulic projects. Advances in Science and Technology of Water Resources, 2006, 26(3): 78-81(in Chinese with English abstract).
21 Pite H D, Topham D R, van Hardenberg B J. Laboratory Measurements of the Drag Force on a Family of Two-Dimensional Ice Keel Models in a Two-Layer Flow. Journal of Physical Oceanography, 1995, 25(12): 3008-3031.
22 Wadhams P. Ice in the ocean. Gordon and Breach Science Publishers, 2000, 170-171.
23 Wadhams P, Mclaren A S, Weintraub R. Ice thickness distribution in Davis Strait in February from submarine sonar profiles. Journal of Geophysical Research, 1985, 90(C1): 1069-1077. doi: 10.1029/JC090iC01p01069.
24 Robert A S, Clifford L R. Extraction of marginal ice zone thickness using gravity wave imagery. Journal of Geophysical Research, 1994, 99(C1):901-918. doi: 10.1029/93JC01956.
25 Yan C. Methods and applications on computational fluid dynamics. Beijing: Beijing University of Aeronautics and Astronautics Press, 2006(in Chinese).
26 Deng J, Ke C Q, Lei R B, et al. Monitoring the motion of Arctic sea-ice and its changes in summer and winter 2009. Chinese Journal of Polar Research, 2013, 25(1): 96-104(in Chinese with English abstract).
27 Steele M, Morison J H, Untersteiner N. The Partition of air-ice-ocean momentum exchange as a function of ice concentration, floe size, and draft. Journal of Geophysical Research, 1989, 94(C9): 12739-12750. doi:10.1029/JC094iC09p12739.
28 Bruce R M, Donald F Y, Theodore H O. Fundamentals of fluid mechanics. John Wiley & Sons Press, 2005, 573-592.
29 Bai Y L, Li Z J, Lu P, et al. Optimization and identification on current drag coefficient of isolated ice floe. Chinese Journal of Polar Research, 2006, 18(2): 108–114(in Chinese with English abstract).
30 Yue Q J, Ji S Y, Bi X J, et al. Determination of computing coefficient for the sea ice numerical model of the Bohai sea. Marine Forecasts, 1999, 16(3):97-103(in Chinese with English abstract).
31 Ji S Y, Wang R X, Bi X J, et al. Determining method of ice drag coefficient. Journal of Glaciology and Geocryology, 2003, 25(suppl.2): 299-303(in Chinese with English abstract).